AIMS Biophysics

AIMS Biophysics, 13(1): 111−130.
DOI: 10.3934/biophy.2026007
Received: 03 December 2025
Revised: 05 March 2026
Accepted: 10 March 2026
Published: 20 March 2026

http://www.aimspress.com/journal/biophysics

*Research article*

# Voronoi diagram-based compensation of preferred particle orientations in cryo-EM 3D reconstructions

**Igor M. Orlov[1,2,3,4] and Bruno P. Klaholz[1,2,3,4]***

[1] Centre for Integrative Biology (CBI), Department of Integrated Structural Biology, IGBMC, CNRS, Inserm, Université de Strasbourg, 1 rue Laurent Fries, 67404 Illkirch, France
[2] Institute of Genetics and of Molecular and Cellular Biology (IGBMC), 1 rue Laurent Fries, Illkirch, France
[3] Centre National de la Recherche Scientifique (CNRS), UMR 7104, Illkirch, France
[4] Institut National de la Santé et de la Recherche Médicale (Inserm), U964, Illkirch, France
[5] Université de Strasbourg, Illkirch, France

* **Correspondence:** Email: klaholz@igbmc.fr; Tel: +33369485278.

**Abstract:** To reveal functional properties of biological complexes using single-particle cryo electron microscopy (cryo-EM), it is important to obtain maps without distortions. 3D reconstructions can be obtained from back-projection of the individual 2D projections of the particles, a concept that assumes equally distributed orientations. However, most biological samples exhibit preferential views due to preferred particle orientations, e.g., at the air–water interface or on a carbon surface of a cryo-EM grid. Here, we present a method based on Voronoi diagrams that takes into account the Euler angle distribution of particles through individual image weighting, thus reducing 3D reconstruction artefacts emanating from preferential particle orientations. Voronoi diagrams are built from the Euler angle values plotted on a sphere in order to graphically display particle orientations, and the assignment of the projection weights is then calculated, being proportional to the individual Voronoi polygon areas. We implemented this real-space approach into a 3D reconstruction routine that allows performing automated weighting. The method was validated using a back-projection algorithm on synthetic model data and on real experimental data with different point group symmetries and in the presence or absence of preferential views, revealing a particular benefit for asymmetric objects.

**Keywords:** single-particle cryo electron microscopy; cryo-EM; 3D reconstruction; Voronoi diagram; back-projection; preferred particle orientations; preferential views; Euler angle distribution; weighting

## 1. Introduction

Single-particle cryo electron microscopy (cryo-EM) comprises several steps during image processing, including particle selection and angle assignment, among others (reviewed in [1–7]). Among these, 3D reconstruction is a key step during which the 3D object is reconstituted. During this step, it is crucial to avoid errors or artefacts that could otherwise affect the interpretability of the resulting cryo-EM map. The essence of single-particle analysis is the usage of many different images of individual molecules to reconstruct a 3D distribution of the object densities, assuming that each image is a projection of the same object [8,9]. Although the mathematical concept of restoring the 3D density from object projections was described more than a century ago [10], it was considered for a long time as a sophisticated theoretical abstraction. Later, this theory found many applications for reconstruction algorithms in the cryo-EM field [11–14]. These approaches share the key assumption that while the distribution of viewing angles of the object is random (Euler angles are represented on a sphere called "Euler sphere"), it can usually be considered even. However, due to uneven particle orientations, this assumption is often imprecise in practice and can lead to severe distortions in the 3D reconstruction if left uncorrected, and make map interpretation imprecise, difficult, or even impossible depending on the degree of distortions.

Image analysis in cryo-EM requires numerically stable and computationally effective methods so that large data sets can be processed to produce 3D reconstructions at near atomic resolution [15–22]. The quality of the 3D reconstruction depends on different parameters such as image quality and particle number in a given data set, the accuracy of the image alignment and angle assignment of the particle images, the symmetry of the object, and whether there is an even angular distribution of the particle views. Sample preparation techniques such as negative staining or plunge-freezing in liquid ethane lead to the fixation of the orientations of the molecules on the carbon surface of an EM grid or embedded in amorphous ice [1,23]. Because molecular positions are fixed in the vitreous ice, the image of a complex is related to the orientation of the molecule with respect to the electron beam. This property allows using the projections of the fixed molecules during the 3D reconstruction procedure. The cryo-EM sample preparation has the advantage of preserving the molecules in a hydrated, functional state as compared to negatively stained samples. However, the cryo-preparation does not by itself ensure an even distribution of views, due to the biophysical properties of biological samples. Indeed, hydrophobic areas on the molecule surface may lead to preferential orientations toward the air–water interface (visible, e.g., by electron tomography [24]) within the thin liquid film that spans holes in holey carbon (unsupported) or that lies on a thin carbon film (carbon-supported). The existence of preferential orientations leads to an overemphasis of densities in this direction in the 3D reconstruction and creates distortions of the structural features. Because uneven distributions of the particle orientations occur commonly with various biological samples, they should be taken into account and compensated for when performing 3D reconstructions. Among different possible solutions that have been suggested, the most frequently implemented method is the exact filtered back-projection approach [12]. In the original sense, weighted back-projections relate to the superposition of Fourier-filtered (Fourier-domain weighted) back-projections. This helps to emphasize fine details and suppress

low-frequency halos, which often appear in 3D reconstructions due to the strong overlap of central sections at low spatial frequencies [12]. This Fourier-domain weighting could be replaced by 3D filtering of the obtained 3D map or sharpening, which can be combined with denoising. This approach is rather efficient but tends to leave some residual distortion artefacts in the maps; also, it does not allow handling a heavily distorted distribution of projections. In the past, the use of Voronoi diagrams has been suggested [25], but its implementation in Fourier space, while elegant, remains too computationally time-consuming and difficult to parallelize. Fourier-based 3D operations may, in some instances, become a limiting factor in the context of high-resolution cryo-EM [1,26], which requires fine sampling with small pixel sizes, creating huge arrays. An alternative could be to develop a real-space approach, which would be fully compatible and convenient in an image processing workflow, as it does not require 3D Fourier operations. Here, we propose a new Voronoi-based weighting scheme for 3D reconstructions, which is computationally fast and runs in real space and is also implemented into a 3D reconstruction software, BKPR. To analyze and highlight preferential views in cryo-EM datasets, we also provide a software, Eulerplot, for plotting Euler angle distributions and occurrences.

## 2. Materials and methods

In 3D reconstruction, reducing preferred particle orientations and the resulting map density distortion requires (i) an estimation of Euler angle distribution and (ii) a weighting of the contributing 2D projections, ideally in a precise way, to obtain 3D reconstruction using more evenly distributed particle orientations. The algorithm calculates the spherical Voronoi diagram by computing the convex hull construction. The convex hull of the input points is calculated, which is equivalent to their Delaunay triangulation on the surface of a sphere. The Delaunay triangulation neighbor information is then used to order the Voronoi region vertices. The surface area of spherical polygons is calculated by decomposing them into spherical triangles. The correction of preferred particle orientations is based on down-weighting the number of projections (by a factor corresponding to the inverse ratio of the Voronoi polygon area) that is used for the 3D reconstruction and is done in real space using the back-projection algorithm published earlier [27]. This is done once the Euler angles have been assigned in the image processing workflow; further refinement of the structure using the corrected 3D reconstruction as an internal reference then allows further refinement of all refinement parameters (such as translational and rotational particle alignments, Euler angle assignments, etc.), resulting in improved cryo-EM map fine features (i.e., with less distortions).

The back-projection and Euler angle image software were written in C++ using the FFTW library (http://www.fftw.org) for the calculation of Fourier transforms and the X11 basic framework for the GUI environment. The software was built using GCC from the GNU compiler collection (https://gcc.gnu.org). The BKPR and Eulerplot software handle image data and can read Euler angles from a text file (with the format of Euler angles alpha, beta, and gamma, which are defined as three subsequent rotations; the first rotation angle alpha describes a rotation around the Z-axis; the next is a rotation along the new Y-axis over the beta angle; finally, the gamma rotation is a rotation around the new Z-axis; all rotations are counter-clockwise).

For the synthetic model data, we used the atomic structure of the 30S small ribosomal subunit from *T. thermophilus* [28] to model the effects of a non-uniform particle distribution. For this, we converted the atomic structure (PDB ID: 1YL4) into a density map in a cube of 512 voxels with a

sampling of 1 Å per pixel using the Gaussian approximation of the atoms with the IMAGIC software [29]. The non-uniform distribution of projections was then simulated using 256 projections of the map. The preferential orientation distributions were generated by adding randomly generated uniform distributions and randomly generated distributions in specific angular areas. The structure of heat shock protein (HSP) [30] (PDB ID: 2BYU) with tetragonal symmetry was used to compute 128 projections within the tetrameric asymmetric unit. For real experimental data, we used previously published datasets of the 30S ribosomal subunit [31], the RXR/VDR nuclear receptor [32], and the grapevine fanleaf virus (GFLV) [33].

## 3. Theory

### *3.1. Theoretical consideration of the problem*

The possibility of reconstructing 3D objects from their projections has been proved analytically by J. Radon in 1917, demonstrating that "the object can be reconstructed uniquely from its line projections when all of its line projections are known". However, the Radon theorem does not address the question of how to reconstruct the object from a limited number of projections. The theorem considers projections as integrals of the multi-dimensional function on a manifold of one-dimensional directions and assumes that all projections are ideal, without noise, and with infinite resolution and exact angular sampling.

In practice, because of a limited number of non-ideal projections, the object cannot be reconstructed with maximum precision up to the Nyquist frequency, i.e., the data quantization frequency. Additional inaccuracy is caused by noise in the input data, possible numerical instability of the algorithm implementations, and the limited number of projections. Known 3D reconstruction algorithms work either in real or Fourier spaces and show algorithm-specific properties that act like a transfer function of the reconstruction process. The inaccuracy caused by the algorithms themselves can be interpreted as a point spread function (PSF) that depicts the shape and size of each point in the 3D density map (the cryo-EM map being, in fact, a Coulomb potential or electrostatic potential map [34–37]). The PSF of a registering system describes the response of a detector device during the acquisition of an image of the point, which should correspond to the Dirac δ function in the case of an ideal situation with a system harboring no distortions and no limitations in resolution. The PSF of a 3D object of limited resolution can be described as a Gaussian function with spherical symmetry. In Fourier space, the PSF corresponds to the modulation transfer function (MTF), where amplitude fluctuations represent the space frequencies of the PSF. The PSF itself can be used to account for preferential views as implemented in the IMAGIC software [29] during 3D reconstruction [38,39], which is based on a uniform integration over spherical Fourier shells [12].

Figure 1 shows an example of the effect of preferential particle views on a 3D reconstruction. Two situations are simulated for a dataset of the 30S small ribosomal subunit: a non-uniform and uniform distribution (Figures 1E and 1F, respectively). The comparison of the middle cross-sections of the reconstructed density maps for non-uniform and uniform distributions reveals significant differences between the two 3D reconstructions (Figure 1A/C and 1B/D); the non-uniform distribution of projections results in an artefactual elongation of densities. All features of a 3D reconstruction start losing sharpness, especially in the direction perpendicular to that of the predominant projections. This situation can be interpreted as an elongation (blurring) of the PSF in one direction, which results in a

non-spherical (non-uniform) PSF, while a proper weighting scheme of particle orientations should correct for that and restore a perfectly spherical PSF shape. The elongation of densities or PSF in a non-uniform distribution is caused by the scarcity of certain orientations, while others are overpopulated in the other (preferential) directions. However, a better and more precise method with regard to the individual particle images would be to assign individual weights to the input projections (in practice, this results in down-weighting overrepresented particle orientations). We chose here to use Voronoi diagrams for this purpose. In the following, we describe the concept and its implementation and provide examples with synthetic data and experimental cryo-EM data.

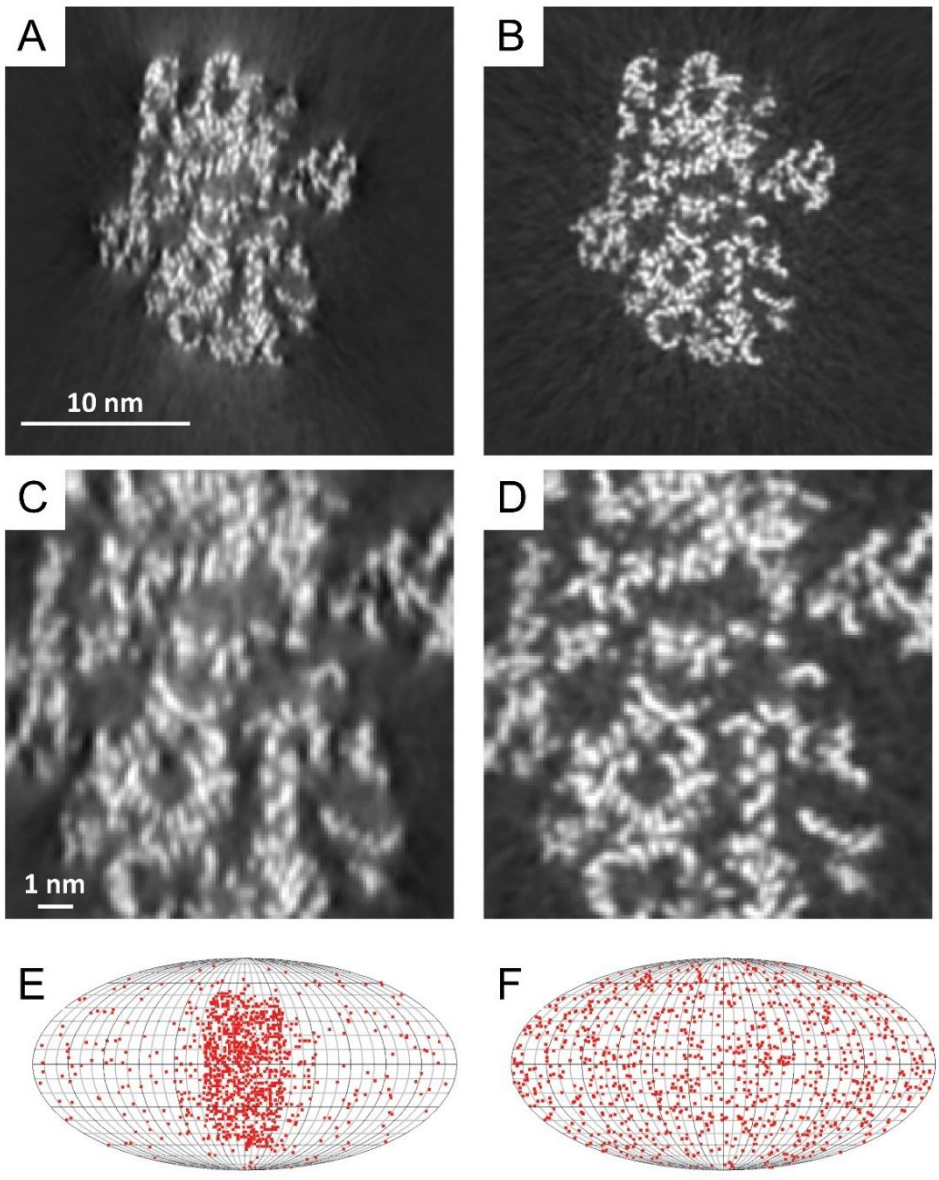


**Figure 1.** 30S small ribosomal subunit test data. A: Central cross-section of the reconstructed 3D density map with preferred orientations (i.e., non-uniform angular distributions). B: Central cross-section of a 3D density map with uniform distribution of projections. C, D: Zoomed regions of panels A and B. E, F: Angular distributions of simulated projections with and without preferential orientations, respectively.

*3.2. Concept of Voronoi diagrams*

Let us first explain the concept of Voronoi diagrams before describing the weighting algorithm used here in cryo-EM 3D reconstructions. The Voronoi diagram on a plane [40,41] is the partitioning of a plane with *n* superposed (generating) points into convex polygons such that each polygon contains exactly one generating point and every plane point inside a given polygon is closer to its generating point than to any other (Figures 2A and B). The generating points are called Voronoi sites. The cells are called Dirichlet regions or Voronoi cells (polygons, open for the outer generating points), and the edges of the cells are called Voronoi edges. A Voronoi diagram is sometimes also known as a Dirichlet tessellation [42]. Each point on the boundary of the Voronoi cell, or a polygon, is equidistant from two Voronoi sites, and each vertex is equidistant from at least three Voronoi sites. As a result, the regions are edge-to-edge and vertex-to-vertex; therefore, all regions form a polygonal partition of the plane without holes or non-partitioned spaces (Figure 2B). Voronoi diagrams are used in various areas and applications, such as for 3D representations and triangulations of objects in computer graphics (e.g., Coot [43], Chimera [44], Pymol [45], etc.), and in many other scientific fields and engineering technologies. Recent applications also include segmentation methods, for example, in super-resolution microscopy for image reconstruction from localization events and clustering analysis of fluorescently labeled macromolecular complexes that we developed recently [46,47]. The dual graph of the Voronoi diagram is the Delaunay triangulation [48,49], which is well known in computer graphics.

The Voronoi diagram on a sphere, which we use to describe the distribution of Euler angles, is similar (equivalent and congruent, but may have open and closed cells) to the diagram on the plane. The link is based on a transformation of a plane into a sphere via, for example, the orthographical transformation. When a set of *n* distinct points is located on the sphere with unit radius and with the center at the origin of the coordinate system [50], the distance between two points *p* and *q* is defined as the length of the shortest arc of the great circle passing through *p* and q (Figure 2C). This distance is called the "great circle distance". The arc that delineates the region of the point dominance between two Voronoi points on the sphere is a great circle that passes through the mid-point of the great circular arc linking *p* and *q* perpendicularly to it. This great circle is equivalent to the Voronoi edge and divides the sphere into two hemispheres. The intersection of hemispheres related to a given site gives the spherical Voronoi region or polygon associated with this site. The set of resulting spherical Voronoi polygons gives a generalized Voronoi diagram, which is called the spherical Voronoi diagram and provides a polygonal tessellation of the unit sphere (Figure 2C), such that the entire sphere is covered without gaps.

We used the concept of the Voronoi diagram on a sphere to assign a weight to each projection according to its region of influence on the Voronoi cell. Each Euler angle of a projection (single-particle image or class average) is represented on the unit sphere as a point of intersection of this sphere with the projection direction (i.e., a Voronoi site) and corresponds to one facet of the Voronoi cell. Each Voronoi cell on the sphere contains one and only one point corresponding to a single projection. Because the area of a cell is inversely proportional to the density of Voronoi sites, a projection weight can be calculated according to the Voronoi cell area in a proportional manner. In other words, the down-weighting of preferential views is inversely proportional to the Voronoi cell area. This results in down-weighting of projections in densely populated areas and up-weighting of projections in sparsely populated areas in order to make stronger use of rare views. In addition, if there are many projections with exactly the same angle, the weight is divided by the number of superimposing or overlapping

projections; this is typical for projection matching, where many images may have an identical angle assignment arising from the corresponding reference image. The determination of the Voronoi diagram on a sphere can be built using Delaunay triangulations. In the procedure described below, the computation of the Voronoi diagram is implemented by carrying out a dual transformation of the Delaunay triangulation.

The Voronoi-based weighting algorithm comprises the following steps:

1. Computation of the Voronoi diagram for the Euler angles of all projections participating in a 3D reconstruction;
2. Computation of the areas of the Voronoi polygons in the Voronoi diagram and usage of their values as real-space weighting factors for individual back-projections (i.e., individual weights are proportional to the individual Voronoi polygon areas);
3. Loading of projections and performing Fourier filtering (Fourier-weighting of projections);
4. Multiplication of all projections with the corresponding real-space weighting factor;
5. Computation of double-weighted (Fourier and Voronoi) 3D reconstruction.

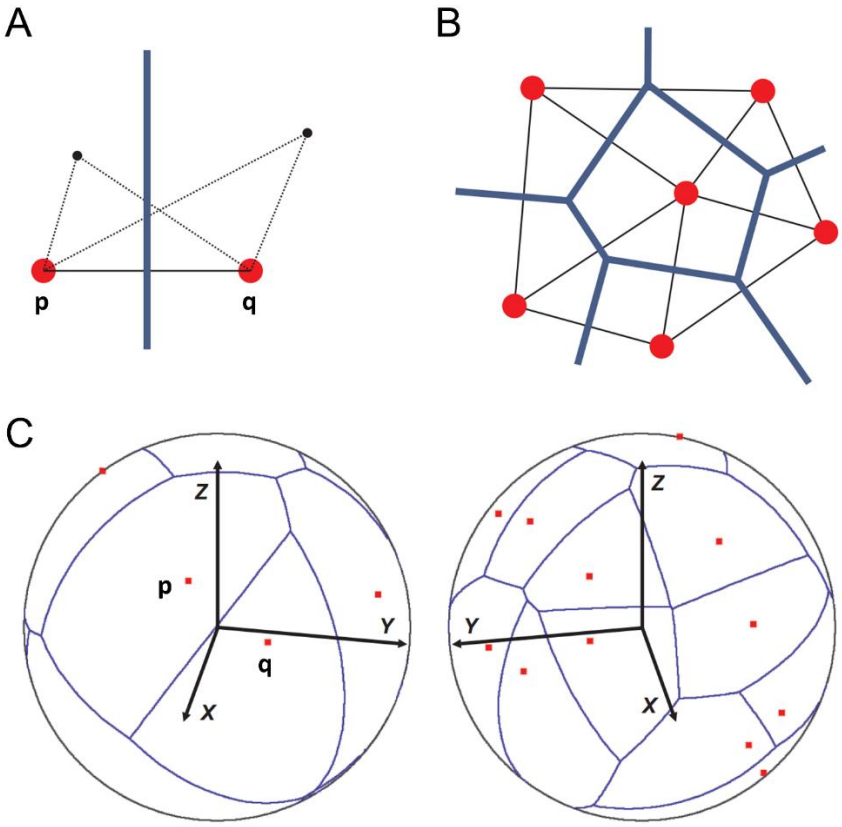


**Figure 2.** Voronoi diagrams on a plane and on a unit sphere. A: Fundamentals of the Voronoi tessellation. Two Voronoi sites (red) and one Voronoi edge (marine blue). B: Voronoi diagram on a plane. Black lines denote Delaunay triangulation. C: Voronoi diagram on a sphere; front and back views (left and right, respectively). The distance (the "great circle distance") between two points *p* and *q* is defined by the length of the shortest arc of the great circle passing through *p* and q; a great circle passes through the midpoint of the great circular arc linking *p* and *q* perpendicularly.

## 4. Results and discussion

The Voronoi-based weighting of particle orientations has been implemented in a software called BKPR (back-projection) and tested on data with different symmetry point groups and with different types of Euler angle distributions (even/uneven), with both synthetic and experimental data. The software analyzes the distribution of projections on the Euler sphere to assign weights for each projection according to the area of the Voronoi polygon on the Euler sphere (Figure 3). In addition, if there are several projections with exactly the same orientation (same Euler angle, which can happen, for example, during angle assignment using projection matching using a reference, but usually not if using common lines and angular reconstitution [51]), the software will treat all these projections as one and down-weight each specific projection according to the total number of projections with the same Euler angle.

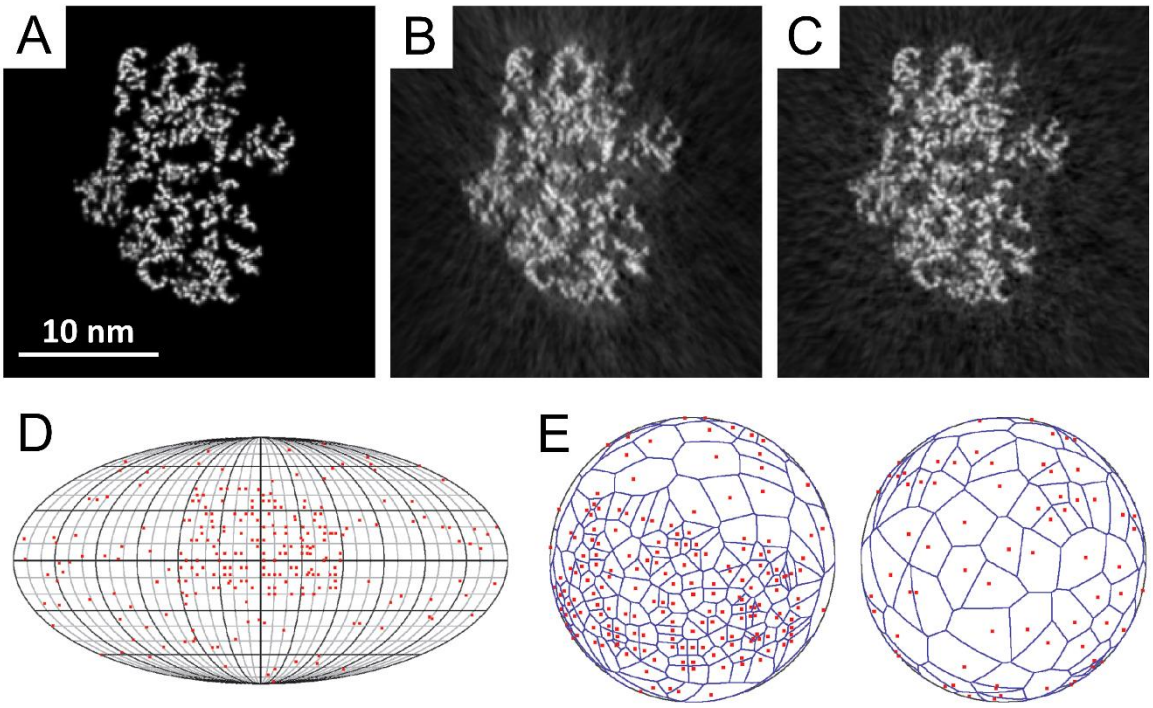


**Figure 3.** Test dataset of the 30S small ribosomal subunit with simulations of preferred orientations. A: Central cross-section of the ideal structure. B, C: Cross-sections of the 3D reconstructions without and with corrections of the preferred orientations, respectively. D, E: 2D and 3D representations (front and back views of the sphere) of the distribution of projections.

We have modeled the effects of a non-uniform particle distribution and its correction by Voronoi weighting using the structure of the 30S small ribosomal subunit (Figures 3 and 4). The dataset has been simulated as a density map of the atomic structure using the Gaussian approximation of the atoms (see Methods). This mimics the typical behavior of a ribosomal specimen on a carbon-supported cryo-EM grid, when the preferential orientation is caused by ribosomes sticking with one side to the carbon. The distribution of projections for this 30S model dataset is shown in 3D (Figure 3E) and as a two-

dimensional distribution on the Euler sphere using our Eulerplot software (Figure 3D; other implementations of angular-equidistant Euler angle plots exist in software such as RELION [52], CryoSPARC [53], or cisTEM [54], a recent distortion-free version being the VUE program that is based on the Lambert azimuthal equal-area projections [55]). Blue lines (Figure 3E) show the corresponding Voronoi diagram on a sphere for this specific distribution of projections, illustrating that the half-sphere with a high density of sampling shows smaller areas of Voronoi polygons, while the opposite half-sphere shows much larger Voronoi polygon areas representing a few rarer views.

The comparison of the reconstructions with the forward projections of the original atomic model demonstrates clear differences between the cross-sections of the "ideal", non-corrected, and corrected structures (Figures 3A–C). While the main features on corrected or non-corrected structures are rather similar, the reconstructions reveal the presence of extra background caused by the limited amount of the rare projections used for model calculations. An increase in the number of projections significantly improves the contrast in the 3D reconstruction as it reduces the background. In the case of a non-even distribution of projections, artefacts appear: in the non-corrected structure, all small elements have the densities elongated (Figure 3B) in the direction where the projection directions are clustered on the Euler sphere (Figure 3D). In the corrected structure, the corresponding areas show fine details without shape distortions (Figure 3C).

We also estimated the influence of the non-uniform distribution of particles on the projections of the structure. Orthogonal projections were computed from the test ribosomal reconstruction shown before, and a comparison was done for three types of 3D reconstructions: ideal, non-corrected, and corrected (Figure 4). The non-uniform distribution of projections is visible mostly in the so-called "front view" of the 30S ribosomal subunit (first column of Figure 4). The "front view" projection from the non-corrected structure exhibits clearly visible elongated traces along the overpopulated direction. The corresponding difference image (Figure 4J–L) clearly shows that the major difference between projections from corrected and non-corrected structures is along a preferential direction, revealing itself through elongated densities along that direction. Moreover, even though for 3D cross-sections of the maps the difference is probably less noticeable, for projections it becomes quite strong (Figure 4D), as illustrated by the corresponding difference image after map subtraction of the ideal reconstruction (Figure 4J). Obviously, if Euler angle assignment and structure refinement are done by projection matching, a certain family of projections could be affected by those 3D reconstruction artefacts. It should also be noted that, in the absence of preferential orientation correction, there is a loss of precise features, as illustrated by the map-model similarity curves calculated by Fourier shell correlation (FSC [56,57]) between the maps and the original atomic coordinates (Figure 5), i.e., the uncorrected maps correlate less well with the atomic model due to the elongation in certain directions, while the corrected maps differ from the atomic model due to the reduced number of input particle projections. While the correction provides more isotropic information with less distortions, the missing information from rare orientations can obviously not be recovered itself (the down-weighting only reduces the dominant orientations).

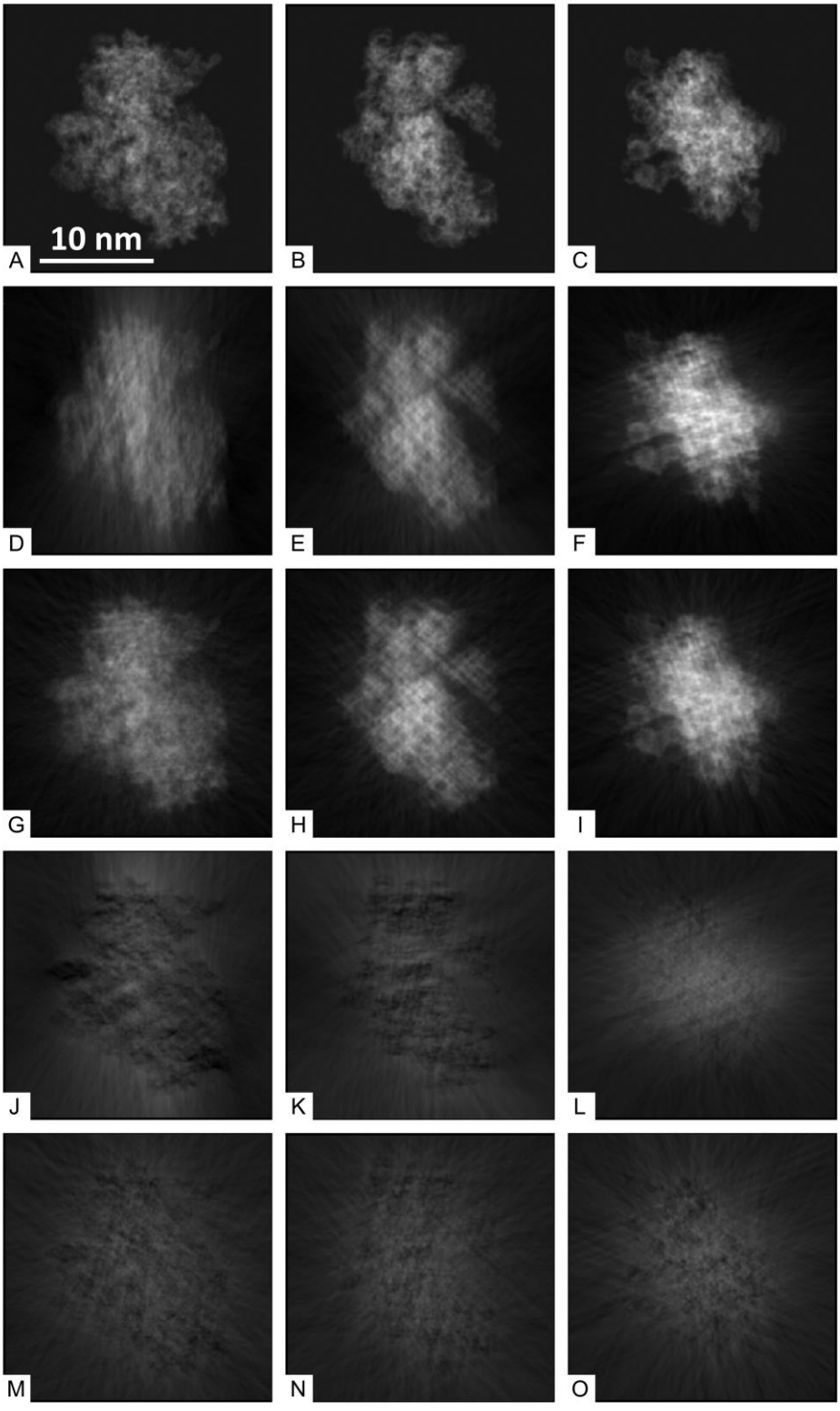


**Figure 4.** Orthogonal projections from the test dataset of the 30S ribosomal subunit. A, B, C: Orthogonal projections from the ideal structure. D, E, F: Orthogonal projections from the non-corrected 3D reconstruction. G, H, I: Orthogonal projections from the corrected 3D reconstruction. J, K, L: Difference mapping between non-corrected and ideal projections. M, N, O: Difference mapping between corrected and ideal projections.

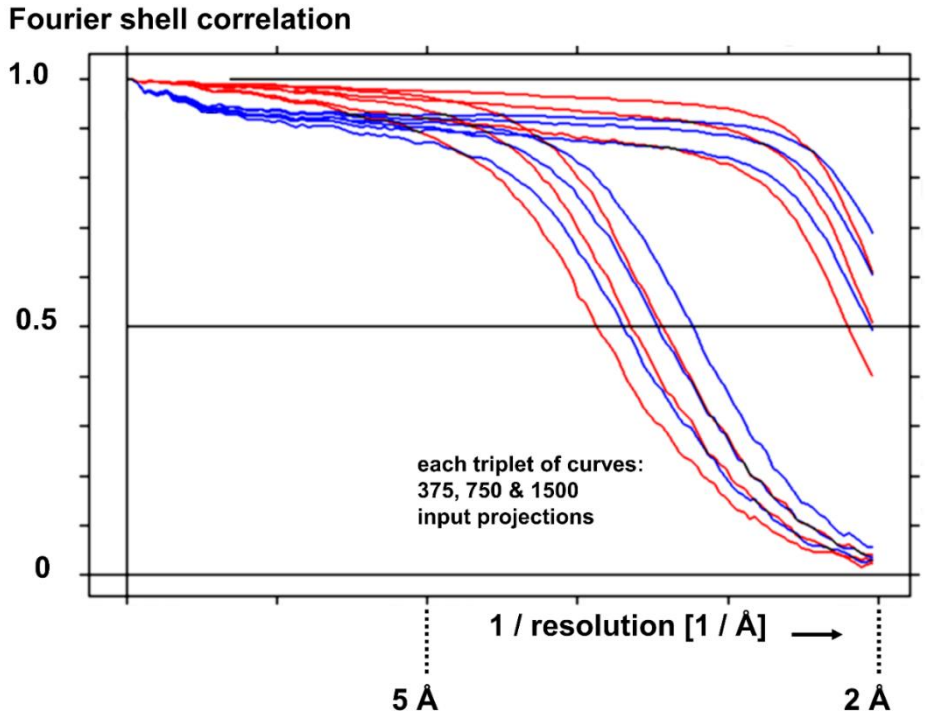


**Figure 5.** Resolution improvement by Voronoi-based weighting of preferred orientations. Map-model similarity curves based on FSC calculations between the atomic model ("ground-truth", as it was used to generate forward projections in the first place) and the 3D reconstructions, showing a net resolution improvement upon Voronoi-based weighting of preferred orientations (left curves: non-corrected reconstructions; right curves: corrected 3D reconstructions) using variable amounts of input projections (from left to right for each set of curves: 375, 750, and 1500 input projections).

To further characterize the Voronoi diagram–based weighting, we also analyzed some typical objects with different levels of internal symmetry. The influence of the non-uniform distribution of projections on the reconstruction of a heat shock protein (HSP) (2BYU) with tetragonal symmetry was monitored by computing 128 projections within the tetrameric asymmetric unit (Figure 6). The strong preferential orientations in one asymmetric unit will be replicated 12 times for the tetrahedral symmetry, resulting in the presence of 12 overweighed directions around the whole sphere instead of one for the asymmetric case. The corresponding Voronoi diagram for all asymmetric units (Figures 6D and E) illustrates that, as can be expected, the high degree of symmetry makes the influence of strong preferential orientations significantly smaller.

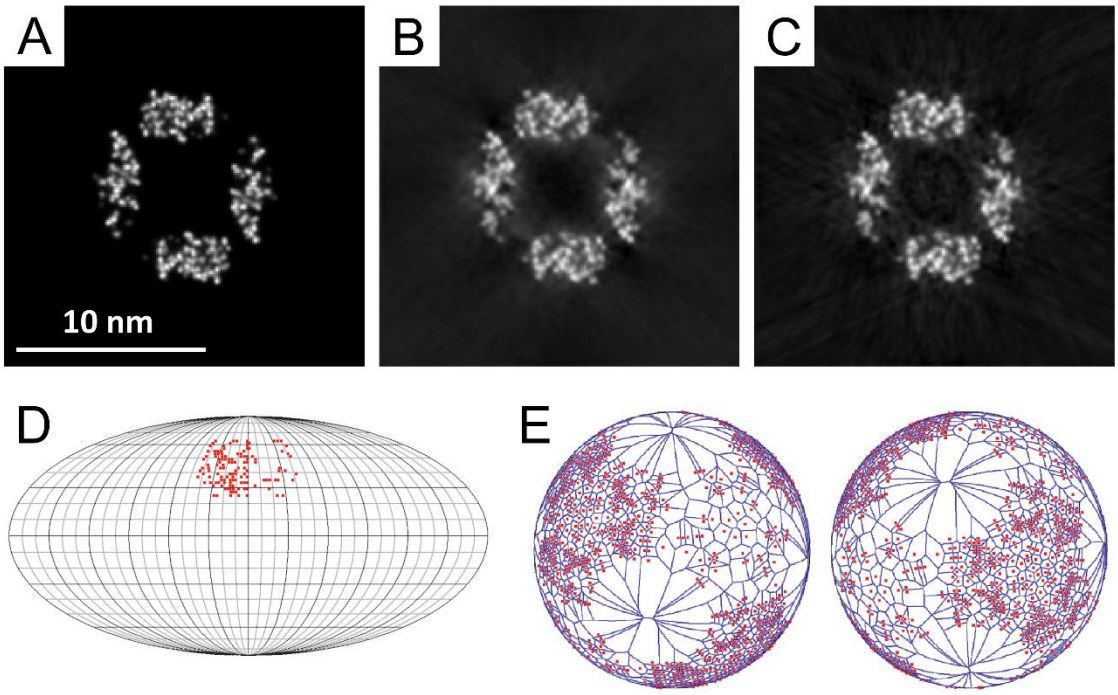


**Figure 6.** Test data and corrected reconstruction for objects with internal symmetry. A: The central cross-section of the ideal structure of the tetrameric heat shock protein. B, C: Cross-sections of the 3D reconstructions without and with correction of preferred orientations, respectively. D, E: 2D and 3D representations (front and back views of the sphere) of the distribution of projections.

## 5. Conclusions

The results described here show that Voronoi-based weighting of projections can help with obtaining 3D reconstructions with fewer distortions. It also shows that our implementation is feasible and numerically stable, an aspect that was not obvious a priori due to the convex nature of Voronoi diagrams (i.e., the lines at edges of Voronoi cells need to be finite; the lines are generated from the intersection of half-planes; Voronoi cells can be closed or open). The synthetic and experimental datasets of asymmetric objects, such as the 30S ribosomal subunit, and symmetric objects, such as HSP, show that the method is applicable to objects with various symmetries. The correction is particularly beneficial for C1 or low-symmetry objects because the asymmetric unit covers the entire Euler sphere, whereas symmetric objects have a small asymmetric unit within which preferential views only marginally affect the quality of the 3D reconstruction. The improvement of the reconstruction with Voronoi-based weighting in comparison with the reconstructions without compensation is visible through the global features and the fine details, which resemble those of the original (ideal) reconstruction, as illustrated also by the difference mapping. There are basically no distortions of the maps (i.e., no stripes in the 3D reconstruction originating from the back projection), as also illustrated by the weak residuals in the difference maps. A clear benefit of the method is that stripy densities get reduced after down-weighting of the preferred particle orientations (Figures 3 and 4). A potential limitation of the method may be that down-weighting of overrepresented views leads to relative up-

weighting of rare views, thereby potentially increasing the noise level in those directions, but this is still better than having those views underrepresented (in the reconstructions done here, we did not observe noise effects, though). Complete absence of views would remain a problem if only the down-weighting of preferred particle orientations is performed. Therefore, cases of extreme preferred orientations may require additional compensation (see alternative methods for down- and upweighting, e.g., using explicit correction of non-uniform distributions [55,58]) or other ways of experimentally acquiring additional views in the cryo-EM data (tilting, changing cryo-EM grid support, adding detergents to the sample before cryo-EM grid preparation, etc.).

In the case of non-uniform particle orientations, there is a significant loss of resolution in one direction of the 3D reconstruction. However, the error is not localized in a specific spatial frequency domain; instead, the resemblance of the structure to the ideal reconstruction is decreased in all frequencies along one direction (i.e., leading to anisotropic resolution). The compensation increases this resemblance to an almost perfect level in the low-frequency domain. However, it slightly reduces the maximum possible resolution due to an increase in high-frequency noise with the relative increase of weights for rare views (the preferential views being down-weighted in the first place). Altogether, however, this is compensated by performing a correction of the preferential orientations, which significantly improves the average volumetric resolution compared to the uncorrected reconstructions, as illustrated by the considerable gain in resolution, which improves from 3.2 to 2.2 Å (based on map-model FSC calculations, Figure 5). The resolution of the map becomes more isotropic, but the nominal average resolution value becomes lower than in the uncorrected, previously strongest direction (which is, in fact, artificially high due to the strong contribution of preferred particle orientation in one direction). Hence, down-weighting of the densely populated particle orientations improves the appearance and detailed features of the map.

A direct evaluation of resolution gain using classical FSC calculations from half-maps turns out to not be the best measure to estimate whether the 3D reconstruction has improved after weighting preferred particle orientations, because they are biased by the number of projections used; with many preferred particle projections, the resolution estimation is artificially higher [58], even though the map is worse in terms of distortions and stripes. Hence, instead of formal resolution estimations, the safest way is to look at map features and perform comparisons with an atomic model (visually to analyze whether map distortions such as stripes in the densities get reduced, complemented by map-model FSC calculations). In practice, the effect of resolution gain may be less strong, but it can be an additional factor for obtaining isotropically resolved cryo-EM maps. This is a crucial parameter that significantly facilitates map interpretation and atomic model building and refinement. Finally, the higher precision of the structure in the low-frequency domain will also facilitate initial 3D reconstructions from relatively few views, thereby increasing the robustness of 3D reconstructions in the early structure determination, in 3D classifications and particle sorting procedures, in focused refinements [5,31,59−66], and in the final refinement steps during image processing. In this context, it is important to note that the usage of an improved 3D reconstruction showing fewer map distortions will be beneficial for the refinement of a structure when that 3D reconstruction is used as the internal reference for further refinement, which will also increase the robustness and precision of angle assignments. In other words, "stripy" maps result in "streaky" references, which, during refinement of the 3D reconstruction, can result in incorrect or imprecise Euler angle assignments. It is well known in image processing that the quality of angle assignments depends on the quality of the structure/map under refinement, and this is particularly true for maximum likelihood–based parameter refinements, which commonly use a

reference. Recent papers and implementations of corrections of preferred particle orientations are based on other methods [55,58,67–72] underlining the novelty of the Voronoi-based weighting concept.

The influence of the weighting decreases when introducing internal symmetries: with higher point group symmetries, the distortions become less pronounced and are almost non-noticeable for icosahedral reconstructions. This is related to the fact that a high-symmetry structure has a smaller asymmetric unit (Figure 6) such that even strong preferential orientations of projections give a rather uniform 3D reconstruction. Indeed, corrections have a rather weak effect in this particular case because symmetric objects do not suffer much from preferential particle orientations due to the small size of the asymmetric unit; a slight particle rotation easily samples the projection angles inside the asymmetric unit within a few degrees, and if the rotation goes beyond that, it is located in the adjacent asymmetric unit, which follows the general symmetry, i.e., it corresponds to an already defined region in the initial asymmetric unit.

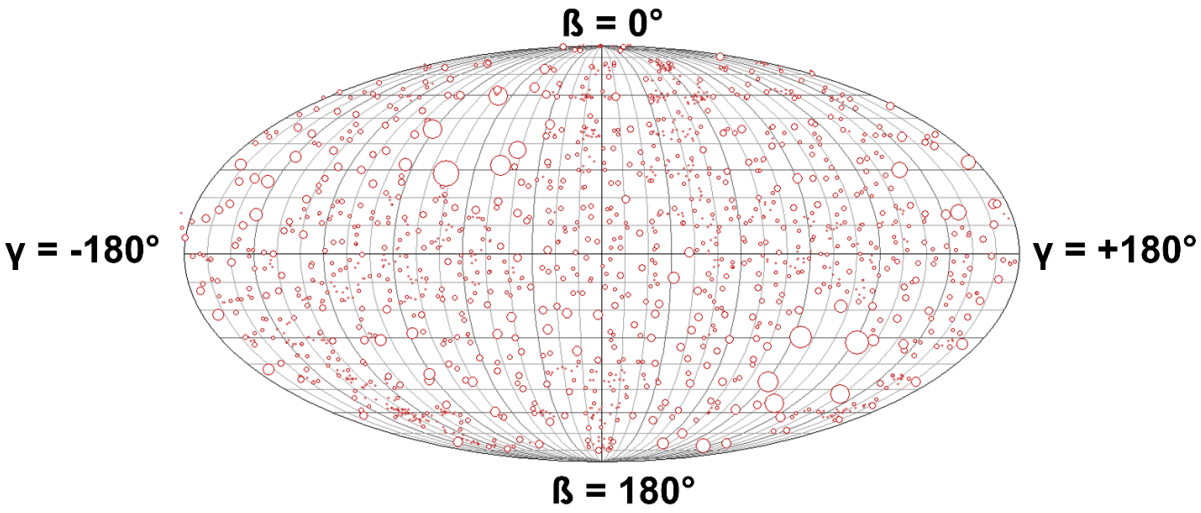


**Figure 7.** Voronoi-based weighting and Eulerplot for the analysis and correction of preferred orientations, as exemplified with experimental data of the DNA-bound RXR/VDR complex. Typical distribution of projection on a unit sphere, as exemplified for the structure of the VDR-RXR-DR3 complex [32]. Circle sizes denote weights, assigned to individual projections according to the Voronoi diagram. The larger the circle size, the stronger the down-weighting assigned to a given projection.

Altogether, we show that the concept of Voronoi-based weighting can be implemented stably and that it behaves robustly for different practical cases of macromolecular complexes. Beyond the synthetic datasets described above, we have also used this method to compensate for preferential particle orientations in experimental data, thus validating our approach and showing its applicability. In the past, we have used this method for determining the 3D reconstructions of several objects, e.g., the 30S ribosomal subunit [31], the RXR/VDR nuclear receptor [32] (both are asymmetric objects), and grapevine fanleaf virus (GFLV) [33] (an icosahedral object), showing its robustness and large applicability. We therefore believe that the concept of Voronoi-based weighting of preferred particle orientations could be used for implementation into future cryo-EM workflows, for which this work lays a conceptual and solid ground. One of the advantages probably stems from the fact that it allows

performing a mathematically precise individual weighting of the input projections, obtaining 3D reconstructions without noticeable residual distortions. In the context of the current high-resolution cryo-EM advent, which can be applied to an increasing number of biological objects, this method will be a useful tool to obtain high-quality 3D reconstructions. This will facilitate cryo-EM map interpretation and atomic model building and refinements, which benefit from less noisy maps and better-defined fine features such as side-chain densities. Finally, the Voronoi-based weighting concept could also be considered for cryo electron tomography (cryo-ET) reconstructions, where it could help with down-weighting and reducing distortions originating from the missing wedge (or missing pyramid in the case of dual-axis cryo-ET [73]). Hence, tilt images closer to zero-tilt would become down-weighted in this case. This could be particularly relevant for objects where no sub-tomogram averaging can be applied, hence relying directly on the 3D reconstruction obtained from the tomogram reconstruction.

Voronoi-based weighting could be particularly useful in the context of on-the-fly image processing and 3D reconstruction, as currently more widely implemented, in particular in the context of infrastructures such as FRISBI or Instruct-ERIC, offering user access to cryo-EM facilities. In this context, the Voronoi-based weighting concept is also convenient for plotting distributions of particle orientations (Figure 7). Hence, the Euler plot software could be useful to analyze the properties of a dataset while image processing is being performed, i.e., during 3D reconstruction and throughout structure refinement, and for data deposition at the EMPIAR and EMDB databases.

## Use of generative-AI tools declaration

The authors declare they have not used Artificial Intelligence (AI) tools in the creation of this article.

## Acknowledgments

We thank our lab members for discussions and suggestions, Alexandre Urzhumtsev for suggestions and Jonathan Michalon for IT support. This work was supported by CNRS (Centre national de la recherche scientifique), Association pour la Recherche sur le Cancer (ARC), Institut National du Cancer (INCa), the Fondation pour la Recherche Médicale (FRM), Ligue nationale contre le cancer (Ligue) and Agence National pour la Recherche (ANR). The electron microscope facility at CBI/IGBMC was supported by the Region Grand Est, FEDER, the French Infrastructure for Integrated Structural Biology (FRISBI) ANR-10-INSB-05-01/France 2030 program, by Instruct-ULTRA as part of the European Union's Horizon 2020 grant ID 731005, by EquipEx$^{+}$ France-Cryo-EM (ANR-21-ESRE-0046) and by Instruct-ERIC.

## Conflict of interest

**The authors declare no conflict of interest.**

## Author contributions

I.M.O. wrote software code, performed image processing and tests with model and real data.

I.M.O. & B.P.K. wrote the manuscript.

## References


1. Orlov I, Myasnikov AG, Andronov L, et al. (2017) The integrative role of cryo electron microscopy in molecular and cellular structural biology. *Biol Cell* 109: 81–93. https://doi.org/10.1111/boc.201600042
2. White HE, Ignatiou A, Clare DK, et al. (2017) Structural study of heterogeneous biological samples by cryoelectron microscopy and image processing. *BioMed Res Int* 2017: 1032432. https://doi.org/10.1155/2017/1032432
3. Costa TRD, Ignatiou A, Orlova EV (2017) Structural analysis of protein complexes by cryo electron microscopy. *Methods Mol Biol* 1615: 377–413. https://doi.org/10.1007/978-1-4939-7033-9_28
4. Earl LA, Falconieri V, Milne JL, et al. (2017) Cryo-EM: beyond the microscope. *Curr Opin Struct Biol* 46: 71–78. https://doi.org/10.1016/j.sbi.2017.06.002
5. von Loeffelholz O, Natchiar SK, Djabeur N, et al. (2017) Focused classification and refinement in high-resolution cryo-EM structural analysis of ribosome complexes. *Curr Opin Struct Biol* 46: 140–148. https://doi.org/10.1016/j.sbi.2017.07.007
6. Chiu W, Downing KH (2017) Editorial overview: Cryo electron microscopy: Exciting advances in cryoEM herald a new era in structural biology. *Curr Opin Struct Biol* 46: iv–viii. https://doi.org/10.1016/j.sbi.2017.07.006
7. Kaelber JT, Hryc CF, Chiu W (2017) Electron cryomicroscopy of viruses at near-atomic resolutions. *Annu Rev Virol* 4: 287–308. https://doi.org/10.1146/annurev-virology-101416-041921
8. De Rosier DJ, Klug A (1968) Reconstruction of three dimensional structures from electron micrographs. *Nature* 217: 130–134. https://doi.org/10.1038/217130a0
9. Klug A (1983) From macromolecules to biological assemblies (Nobel Lecture). *Biosci Rep* 3: 395–430. https://doi.org/10.1002/anie.198305653
10. Radon J (1917) Über die Bestimmung von Funktionen durch ihre Integralwerte langs gewisser Manningfaltigkeiten. (On the determination of functions from their integrals along certain manifolds). *Aka Wiss* 69: 262–277.
11. Herman GT (1980) *Image Reconstruction from Projections: the Fundamentals of Computerized Tomography*, New York: Academic Press.
12. Harauz G, van Heel M (1986) Exact filters for general geometry three dimensional reconstruction. *Optik* 73: 146–156.
13. Russ JC, Neal FB (1995) *The Image Processing Handbook*, Boca Raton: CRC press. https://doi.org/10.1201/b18983
14. Frank J (2006) *Three-Dimensional Electron Microscopy of Macromolecular Assemblies: Visualization of Biological Molecules in Their Native State*, New York: Oxford Academic. https://doi.org/10.1093/acprof:oso/9780195182187.001.0001
15. Bai XC, Fernandez IS, McMullan G, et al. (2013) Ribosome structures to near-atomic resolution from thirty thousand cryo-EM particles. *eLife* 2: e00461. https://doi.org/10.7554/eLife.00461
16. Amunts A, Brown A, Toots J, et al. (2015) Ribosome. The structure of the human mitochondrial ribosome. *Science* 348: 95–98. https://doi.org/10.1126/science.aaa1193

17. Khatter H, Myasnikov AG, Natchiar SK, et al. (2015) Structure of the human 80S ribosome. *Nature* 520: 640–645. https://doi.org/10.1038/nature14427
18. Abeyrathne PD, Koh CS, Grant T, et al. (2016) Ensemble cryo-EM uncovers inchworm-like translocation of a viral IRES through the ribosome. *eLife* 5: e14874. https://doi.org/10.7554/eLife.14874
19. Merk A, Bartesaghi A, Banerjee S, et al. (2016) Breaking cryo-EM resolution barriers to facilitate drug discovery. *Cell* 165: 1698–1707. https://doi.org/10.1016/j.cell.2016.05.040
20. Natchiar SK, Myasnikov AG, Kratzat H, et al. (2017) Visualization of chemical modifications in the human 80S ribosome structure. *Nature* 551: 472–477. https://doi.org/10.1038/nature24482
21. Dai X, Li Z, Lai M, et al. (2017) *In situ* structures of the genome and genome-delivery apparatus in a single-stranded RNA virus. *Nature* 541: 112–116. https://doi.org/10.1038/nature20589
22. Kühlbrandt W (2014) The resolution revolution. *Science* 343: 1443–1444. https://doi.org/10.1126/science.1251652
23. Glaeser RM, Han BG (2017) Opinion: hazards faced by macromolecules when confined to thin aqueous films. *Biophys Rep* 3: 1–7. https://doi.org/10.1007/s41048-016-0026-3
24. Rice WJ, Cheng A, Noble AJ, et al. (2018) Routine determination of ice thickness for cryo-EM grids. *J Struct Biol* 204: 38−44. https://doi.org/10.1016/j.jsb.2018.06.007
25. Penczek PA, Renka R, Schomberg H (2004) Gridding-based direct Fourier inversion of the three-dimensional ray transform. *J Opt Soc Am A* 21: 499–509. https://doi.org/10.1364/JOSAA.21.000499
26. Kühlbrandt W (2014) Cryo-EM enters a new era. *eLife* 3: e03678. https://doi.org/10.7554/eLife.03678
27. Orlov IM, Morgan DG, Cheng RH (2006) Efficient implementation of a filtered back-projection algorithm using a voxel-by-voxel approach. *J Struct Biol* 154: 287–296. https://doi.org/10.1016/j.jsb.2006.03.007
28. Jenner L, Romby P, Rees B, et al. (2005) Translational operator of mRNA on the ribosome: how repressor proteins exclude ribosome binding. *Science* 308: 120–123. https://doi.org/10.1126/science.1105639
29. van Heel M, Harauz G, Orlova EV, et al. (1996) A new generation of the IMAGIC image processing system. *J Struct Biol* 116: 17–24. https://doi.org/10.1006/jsbi.1996.0004
30. Kennaway CK, Benesch JLP, Gohlke U, et al. (2005) Dodecameric structure of the small heat shock protein Acr1 from Mycobacterium tuberculosis. *J Biol Chem* 280: 33419–33425. https://doi.org/10.1074/jbc.M504263200
31. Simonetti A, Marzi S, Myasnikov AG, et al. (2008) Structure of the 30S translation initiation complex. *Nature* 455: 416–420. https://doi.org/10.1038/nature07192
32. Orlov I, Rochel N, Moras D, et al. (2012) Structure of the full human RXR/VDR nuclear receptor heterodimer complex with its DR3 target DNA. *EMBO J* 31: 291–300. https://doi.org/10.1038/emboj.2011.445
33. Orlov I, Hemmer C, Ackerer L, et al. (2020) Structural basis of nanobody recognition of grapevine fanleaf virus and of virus resistance loss. *Proc Natl Acad Sci USA* 117: 10848–10855. https://doi.org/10.1073/pnas.1913681117
34. Hryc CF, Chen DH, Afonine PV, et al. (2017) Accurate model annotation of a near-atomic resolution cryo-EM map. *Proc Natl Acad Sci USA* 114: 3103–3108. https://doi.org/10.1073/pnas.1621152114

35. Wang J, Moore PB (2017) On the interpretation of electron microscopic maps of biological macromolecules. *Protein Sci* 26: 122–129. https://doi.org/10.1002/pro.3060
36. Wang J, Natchiar SK, Moore PB, et al. (2021) Identification of $Mg^{2+}$ ions next to nucleotides in cryo-EM maps using electrostatic potential maps. *Acta Crystallogr Sect Struct Biol* 77: 534–539. https://doi.org/10.1107/S2059798321001893
37. Bick T, Dominiak PM, Wendler P (2024) Exploiting the full potential of cryo-EM maps. *BBA Adv* 5: 100113. https://doi.org/10.1016/j.bbadva.2024.100113
38. Ray P, Klaholz BP, Finn RD, et al. (2003) Determination of *Escherichia coli* RNA polymerase structure by single particle cryoelectron microscopy. *Method Enzymol* 370: 24–42. https://doi.org/10.1016/S0076-6879(03)70003-2
39. van Heel M, Gowen B, Matadeen R, et al. (2000) Single-particle electron cryo-microscopy: towards atomic resolution. *Q Rev Biophys* 33: 307–369. https://doi.org/10.1017/s0033583500003644
40. Voronoi G (1907) Nouvelles applications des paramètres continus à la théorie des formes quadratiques. *J Reine Angew Math* 133: 97−178. https://doi.org/10.1515/crll.1908.133.97
41. Aurenhammer F, Klein R (2000) *Handbook of Computational Geometry*, Amsterdam, Netherlands: North-Holland, 201−290.
42. Dirichlet GL (1850) Über die Reduktion der positiven quadratischen Formen mit drei unbestimmten ganzen Zahlen. *J Reine Angew Math* 40: 209−227. https://doi.org/10.1515/crll.1850.40.209
43. Emsley P, Lohkamp B, Scott WG, et al. (2010) Features and development of Coot. *Acta Crystallogr D Biol Crystallogr* 66: 486–501. https://doi.org/10.1107/S0907444910007493
44. Pettersen EF, Goddard TD, Huang CC, et al. (2004) UCSF Chimera--a visualization system for exploratory research and analysis. *J Comput Chem* 25: 1605–1612. https://doi.org/10.1002/jcc.20084
45. DeLano WL, The PyMOL Molecular Graphics System (DeLano Scientific), 2002. Available from: http://www.pymol.org.
46. Andronov L, Orlov I, Lutz Y, et al. (2016) ClusterViSu, a method for clustering of protein complexes by Voronoi tessellation in super-resolution microscopy. *Sci Rep* 6: 24084. https://doi.org/10.1038/srep24084
47. Andronov L, Michalon J, Ouararhni K, et al. (2018) 3DClusterViSu: 3D clustering analysis of super-resolution microscopy data by 3D Voronoi tessellations. *Bioinformatics* 34: 3004−3012. https://doi.org/10.1093/bioinformatics/bty200
48. Delaunay B (1928) Sur la sphère vide. *Proc Int Math Congr* 695–700.
49. Delaunay B (1934) Sur la sphère vide. *Izv Akad Nauk SSSR Otd Mat Estestv Nauk* 793–800.
50. Okabe A, Boots B, Sugihara K, et al. (2000) *Spatial Tessellations: Concepts and Applications of Voronoi Diagrams*, 2 Eds., Chichester: Wiley.
51. van Heel M (1987) Angular reconstitution: a posteriori assignment of projection directions for 3D reconstruction. *Ultramicroscopy* 21: 111–123. https://doi.org/10.1016/0304-3991(87)90078-7
52. Scheres SHW (2012) RELION: implementation of a Bayesian approach to cryo-EM structure determination. *J Struct Biol* 180: 519–530. https://doi.org/10.1016/j.jsb.2012.09.006
53. Punjani A, Rubinstein JL, Fleet DJ, et al. (2017) cryoSPARC: algorithms for rapid unsupervised cryo-EM structure determination. *Nat Methods* 14: 290–296. https://doi.org/10.1038/nmeth.4169

54. Grant T, Rohou A, Grigorieff N (2018) cisTEM, user-friendly software for single-particle image processing. *eLife*: 7e35383. https://doi.org/10.7554/eLife.35383
55. Urzhumtseva L, Barchet C, Klaholz BP, et al. (2024) Program VUE: analysing distributions of cryo-EM projections using uniform spherical grids. *J Appl Crystallogr* 57: 865–876. https://doi.org/10.1107/S1600576724002383
56. van Heel M, Keegstra W, Schutter WG, et al. (1982) Arthropod hemocyanin studied by image analysis. *Life Chem Rep Suppl* 1: 5.
57. Saxton WO, Baumeister W (1982) The correlation averaging of a regularly arranged bacterial cell envelope protein. *J Microsc* 127: 127–138. https://doi.org/10.1111/j.1365-2818.1982.tb00405.x
58. Barchet C, von Loeffelholz O, Bahena-Ceron R, et al. (2026) Explicit correction of severely non-uniform distributions of cryo-EM views. *Acta Crystallogr Sect Struct Biol* 82: 65−78. https://doi.org/10.1107/S2059798326000306
59. Klaholz BP, Myasnikov AG, van Heel M (2004) Visualization of release factor 3 on the ribosome during termination of protein synthesis. *Nature* 427: 862–865. https://doi.org/10.1038/nature02332
60. White HE, Saibil HR, Ignatiou A, et al. (2004) Recognition and separation of single particles with size variation by statistical analysis of their images. *J Mol Biol* 336: 453–460. https://doi.org/10.1016/j.jmb.2003.12.015
61. Penczek PA, Frank J, Spahn CMT (2006) A method of focused classification, based on the bootstrap 3D variance analysis, and its application to EF-G-dependent translocation. *J Struct Biol* 154: 184–194. https://doi.org/10.1016/j.jsb.2005.12.013
62. Scheres SHW (2010) Classification of structural heterogeneity by maximum-likelihood methods. *Methods Enzymol* 482: 295–320. https://doi.org/10.1016/S0076-6879(10)82012-9
63. Klaholz BP (2015) Structure sorting of multiple macromolecular states in heterogeneous cryo-EM samples by 3D multivariate statistical analysis. *Open J Stat* 5: 820−836. https://doi.org/10.4236/ojs.2015.57081
64. Barchet C, Fréchin L, Holvec S, et al. (2023) Focused classifications and refinements in high-resolution single particle cryo-EM analysis. *J Struct Biol* 215: 108015. https://doi.org/10.1016/j.jsb.2023.108015
65. Holvec S, Barchet C, Lechner A, et al. (2024) The structure of the human 80S ribosome at 1.9 Å resolution reveals the molecular role of chemical modifications and ions in RNA. *Nat Struct Mol Biol* 31: 1251−1264. https://doi.org/10.1038/s41594-024-01274-x
66. Fréchin L, Holvec S, von Loeffelholz O, et al. (2023) High-resolution cryo-EM performance comparison of two latest-generation cryo electron microscopes on the human ribosome. *J Struct Biol* 215: 107905. https://doi.org/10.1016/j.jsb.2022.107905
67. Urzhumtsev AG (2026) Quantifying distributions of cryo-EM projections. *Acta Crystallogr Sect Struct Biol* 82: 100–112. https://doi.org/10.1107/S2059798325011611
68. Zhu D, Cao W, Li J, et al. (2024) Correction of preferred orientation-induced distortion in cryo-electron microscopy maps. *Sci Adv* 10: eadn0092. https://doi.org/10.1126/sciadv.adn0092
69. Liu YT, Fan H, Hu JJ, et al. (2025) Overcoming the preferred-orientation problem in cryo-EM with self-supervised deep learning. *Nat Methods* 22: 113–123. https://doi.org/10.1038/s41592-024-02505-1
70. Yan Y, Fan S, Yuan F, et al. (2026) A comprehensive foundation model for cryo-EM image processing. *Nat Methods* 23: 88–95. https://doi.org/10.1038/s41592-025-02916-8

71. Zhang H, Zheng D, Wu Q, et al. (2025) CryoPROS: Correcting misalignment caused by preferred orientation using AI-generated auxiliary particles. *Nat Commun* 16: 4565. https://doi.org/10.1038/s41467-025-59797-w
72. Sorzano COS, Semchonok D, Lin SC, et al. (2021) Algorithmic robustness to preferred orientations in single particle analysis by CryoEM. *J Struct Biol* 213: 107695. https://doi.org/10.1016/j.jsb.2020.107695
73. Myasnikov AG, Afonina ZA, Klaholz BP (2013) Single particle and molecular assembly analysis of polyribosomes by single- and double-tilt cryo electron tomography. *Ultramicroscopy* 126: 33–39. https://doi.org/10.1016/j.ultramic.2012.12.009

AIMS Press

© 2026 the Author(s), licensee AIMS Press. This is an open access article distributed under the terms of the Creative Commons Attribution License (http://creativecommons.org/licenses/by/4.0)